Spinal Cord Explants Use Carbon Nanotube Interfaces To Enhance Neurite Outgrowth and To Fortify Synaptic Inputs

Alessandra Fabbro,[†,⊥] Ambra Villari,[†,⊥] Jummi Laishram,[†] Denis Scaini,[†,‡] Francesca M. Toma,[§] Antonio Turco,[§] Maurizio Prato,[§,*] and Laura Ballerini[†,*]

[†]Life Science Department, Center for Neuroscience B.R.A.I.N., University of Trieste, via Giorgieri 1, I-34127 Trieste, Italy, [‡]SENIL, ELETTRA Synchrotron Light Source, I-34127 Trieste, Italy, and [§]Department of Chemical and Pharmaceutical Sciences, University of Trieste, Piazzale Europa 1, I-34127 Trieste, Italy. [⊥]These authors contributed equally to this work.

ABSTRACT New developments in nanotechnology are increasingly designed to modulate relevant interactions between nanomaterials and neurons, with the aim of exploiting the physical properties of synthetic materials to tune desired and specific biological processes. Carbon nanotubes have been applied in several areas of nerve tissue engineering to study cell behavior or to instruct the growth and organization of neural networks. Recent reports show that nanotubes can sustain and promote electrical activity in networks of cultured neurons. However, such results are usually limited to carbon nanotube/neuron hybrids formed on a monolayer of dissociated brain cells. In the present work, we used organotypic spinal slices to model multilayer tissue complexity, and we interfaced such spinal segments to carbon nanotube scaffolds for weeks. By immunofluorescence, scanning and transmission electronic microscopy, and atomic force microscopy, we investigated nerve fiber growth when neuronal processes exit the spinal explant and develop in direct contact to the substrate. By single-cell electrophysiology, we investigated the synaptic activity of visually identified ventral interneurons, within the ventral area of the explant, thus synaptically connected, but located remotely, to the substrate/network interface. Here we show that spinal cord explants interfaced for weeks to purified carbon nanotube scaffolds expand more neuronal fibers, characterized by different mechanical properties and displaying higher growth cones activity. On the other hand, exploring spontaneous and evoked synaptic activity unmasks an increase in synaptic efficacy in neurons located at as far as 5 cell layers from the cell–substrate interactions.

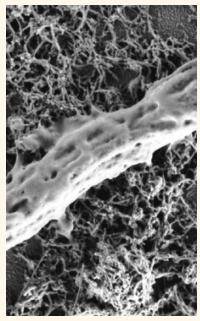

KEYWORDS: nanoscaffold · tissue engineering · organotypic cultures · electrical stimulation · growth cone · patch clamp · postsynaptic current

The exploration of hybrid devices where, for example, single neurons or neuronal networks are grown integrated to conductive nanomaterials[1−11] is increasingly attracting neuroscientists' curiosity.[12,13] Indeed, driven by the limited reparative ability of the central nervous system (CNS), recent research approaches have increasingly focused on the physical factors that, at the interface between cells and material,[14−19] may improve or guide functional recovery of the damaged tissue.[12,18] Such a strategy is generally accepted as complementary to the design of new nanostructures to accomplish (nerve) tissue reconstruction.[12,13,18,20,21]

Interdisciplinary research in modern neuroscience allows one to obtain hybrid circuits *via* assembling nanomaterials, with known physical-chemical properties, and cultured neurons.[3,5−11] By such devices, we can examine how manufactured physical features are sensed by cells, which molecular machineries are activated, and how the emerging signaling is translated into tissue-specific instructions in CNS development, disease, and repair.[9,15,17,19]

In line with these approaches, we recently crafted conductive meshworks of purified carbon nanotubes to sustain cultured neuron growth.[5,6] Carbon nanotubes exhibit unusual mechanical strength coupled with remarkable flexibility; in addition, depending on their structure, they feature large electrical conductivity, allowing nanotubes to conduit electrical current between electrochemical interfaces, leading to the design of a variety of miniaturized devices with unique properties.[22−25] More recently, carbon nanotubes have attracted increasing attention for the development of nano–bio hybrid systems able to govern cell-specific behaviors in cultured neuronal networks.[3,5,6,26−29] Carbon nanotube–neuron hybrid networks always display a boost in signal transmission, detected as an increase in synaptic event frequency.[4,28] We recently reported that direct nanotube–substrate interactions

* Address correspondence to lballerini@units.it, prato@units.it.

Received for review September 13, 2011 and accepted February 16, 2012.

Published online February 16, 2012
10.1021/nn203519r

with the membranes of neurons can affect single neuron activity[5] and promote network connectivity and synaptic plasticity in mammalian cortical circuits in culture.[6] The nature of the interactions between carbon nanotubes and cell membranes is still elusive, although electrical and physical mechanisms have been suggested.[5,30,31]

Despite these interesting findings, studies involving more complex tissue models are still missing; in fact, all known effects (on neuronal development or on neuronal signaling) of conductive nanofibers are limited to carbon nanotube/neuronal hybrids formed on a monolayer of dissociated brain cells.[3,5,6,8,26−29]

Here we use organotypic cultures of the embryonic mouse spinal cord interfaced for weeks with carbon nanotube scaffolds to investigate whether and how the interactions at the monolayer level are translated to multilayered nerve tissues. Organotypic spinal slices represent a biological model of segmental microcircuits, which can be directly investigated at different growth time *in vitro*.[32] In the present work, we combine immunofluorescence, confocal microscopy, scanning and transmission electron microscopy (SEM and TEM), atomic force microscopy (AFM), and single-cell electrophysiology to investigate the growth, the morphology, and the adhesion of neuronal processes exiting the cultured spinal segments when interfaced to carbon nanotubes, together with the dynamics of the electrical signaling within the multilayered spinal networks. Long-term interfacing spinal cord explants to purified carbon nanotubes induces two major effects: (i) an increase in the number and length of neuronal fibers outgrowing the spinal segment, associated with changes in growth cone activity and in fiber elastomechanical properties; (ii) in spinal networks, synaptic currents, either evoked upon afferent stimulations or spontaneously generated, display a significant increase in amplitude, indicating an augment in synaptic responses even in neurons located at as far as 5 cell layers from the cell−substrate interactions. We propose that these two effects rely on direct and indirect MWCNT interactions: the first being mediated by direct adhesion of outgrowing fibers to the nanostructured carbon substrate; the second by alterations in the activity of neuronal layers interfaced to the substrate, able to influence remote, although synaptically coupled, neuronal ensembles.

RESULTS AND DISCUSSION

We developed artificial nanomaterial-based scaffolds to explore for the first time the semichronic (weeks) impact of carbon nanotube interfaces to spinal segment growth and activity. We adopted a multidisciplinary approach, and we used our recently developed ability to grow neurons directly on purified carbon nanotube layers with the aim of addressing the functional changes taking place in a complex tissue when interfaced to a dense multiwalled carbon nanotube (MWCNT) meshwork characterized by large surface roughness and conductivity.[5,6]

Spinal Cord Explant Growth on Carbon Nanotube Surfaces. We tested the ability of carbon nanotube substrates to interface CNS explant growth by coculturing embryonic spinal cord and dorsal root ganglia (DRG) thin slices on a film of purified MWCNTs for 8−20 days, to allow for tissue growth. MWCNTs were subjected to routine thermal gravimetric analysis (TGA) controls and electron microscopy analysis (see Methods) to assess their degree of purity and of defunctionalization, as previously reported.[6] By scanning the carbon nanotube surface topography, we observed the stable retention of MWCNTs on glass coverslips (see below for scanning electron and atomic force microscopy).

We investigated the morphology and growth of spinal slices on carbon nanotube scaffolds by performing immunofluorescence staining and confocal microscopy in organotypic spinal cultures at 8−10 days of *in vitro* (DIV) growth following dissection. Organotypic slices grown on carbon nanotubes (named CNT slices; $n = 13$ slices) were compared to control ($n = 12$ slices) sister cultures (*i.e.*, cultures derived from the same embryos) sampled at the same age *in vitro*.

Figure 1 shows low-resolution bright-field (A) and phase contrast (B) images of healthy control and CNT slices, respectively. The entire area of tissue growth is visualized, and in both samples, it includes the spinal slice, at the center, and the outgrowing area comprising the DRGs and a dense mesh of neurites in the surrounding outgrowth belt. In the sample of Figure 1, the overall area of growth in the CNT slice tends to be larger (+20% in the total diameter, *i.e.*, center and belt) than the control one. We further dissected the morphology of cultured slices by performing immunofluorescence labeling to visualize the distribution of specific cytoskeletal components, such as F-actin and β-tubulin III, the microtubule component expressed exclusively in neurons. To identify glial cells, the specific marker GFAP was used. In Figure 1, the confocal (low-magnification) image reconstructions of typical control (C) and CNT (D) 8 DIV organotypic slices are shown. Astrocytes were identified by immunofluorescence localization of GFAP, an intermediate filament protein expressed in the astrocyte cytoskeleton. GFAP expression usually increases as the cell matures.[33] In both culture groups, control and CNT, GFAP-positive cells (Figure 1C,D, in green) were confined to the explanted spinal slice, with a rare and limited extension to the proximal area of the surrounding growth belt.[33,34] Also, F-actin labeling distribution was similar in the two samples, control and CNT slices (Figure 1C,D, in red). F-actin labeling was both localized within the slice body and further extended to the surrounding outgrowth area, although uniform labeling remained confined to the proximal area of neuronal processes'

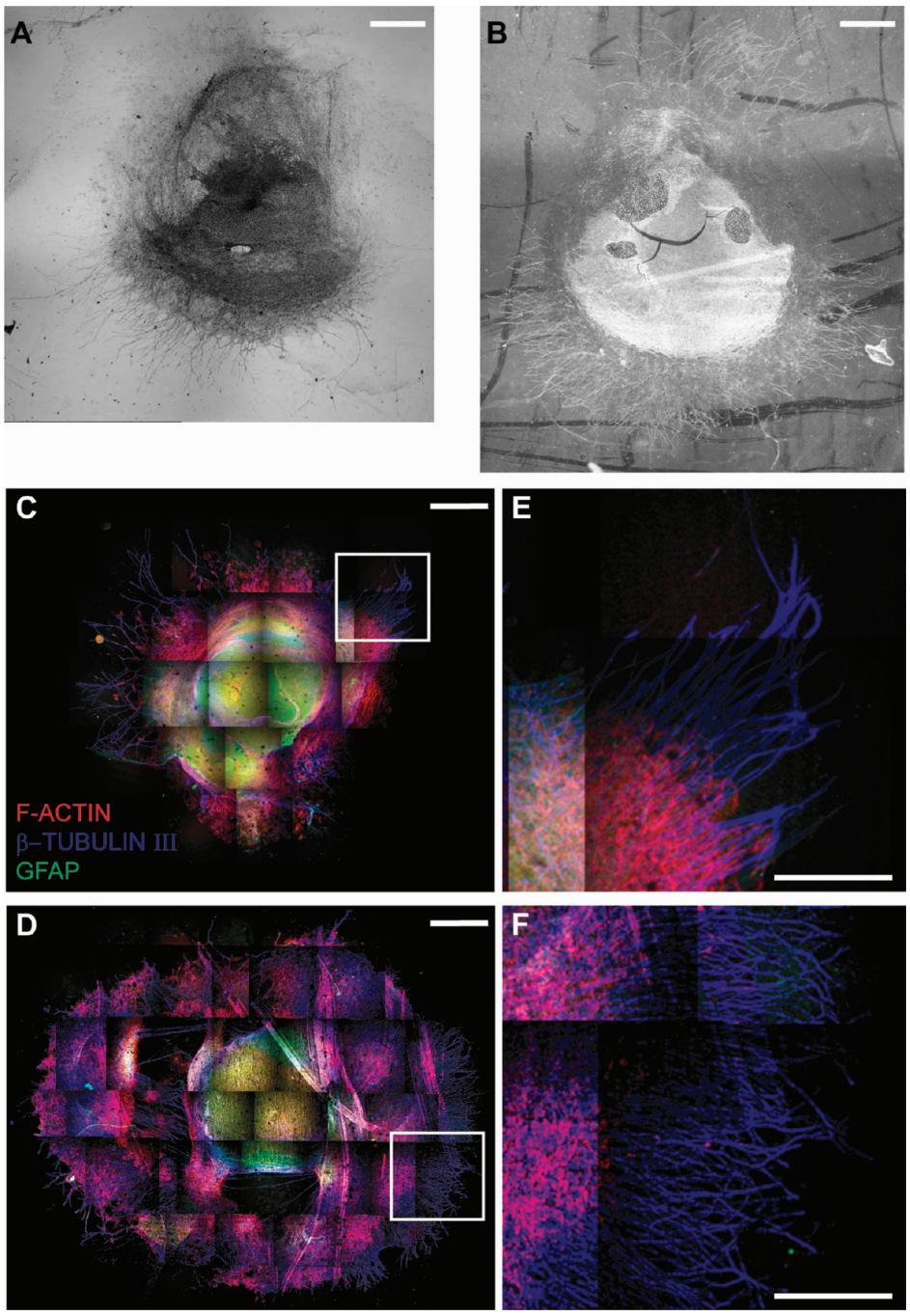

Figure 1. Organotypic spinal cultures: impact of MWCNT interfaces on neurite outgrowth. (A,B) Bright-field and phase contrast images taken after 8 DIV of growth of spinal explants in control and carbon nanotube substrates, respectively. Note that the outgrowth area of the spinal explant tends to be larger (+20%) when interfaced to MWCNTs. (C,D) Confocal image reconstructions of spinal slice cultures at 8 DIV, under control and CNT growth conditions, respectively. Immunofluorescence of specific cytoskeletal components, F-actin, β-tubulin III, and GFAP, was used. Note the β-tubulin III positive neuronal processes radially exiting the growth area in both cultured explants. (E,F) High confocal magnifications of the framed areas highlighted in C and D, respectively, visualizing the bundles of fibers emerging from the growing belt located around the slices. C–F: green, GFAP; red, F-actin; blue, β-tubulin III. In A–D: scale bar 1 mm. In E,F: scale bar 500 μm.

growth, with a punctuate labeling along distal neurites. The distribution of microtubules within the growing slices was visualized by antibody staining for β-tubulin III, specifically localized in the nerve cells, extending into the extremities of neuronal processes and in the small branches located along their length (Figure 1C–F, in blue). At higher magnification, in Figure 1E,F, single as well as bundles (*i.e.*, with >10 μm diameter; see Methods) of β-tubulin III positive neurites extending radially from the surrounding belt of outgrowth are shown for both culture groups, control and CNT, respectively. To quantify the growth of distal neuronal

processes, we co-labeled slices for F-actin and/or GFAP and for β-tubulin III, and we measured the number of β-tubulin III positive bundles exiting at least 150−200 μm from the edge of the surrounding belt. CNT slices were characterized by a significant increase (+ 39%; $P < 0.05$) in the number of distal β-tubulin III positive processes when compared to controls (from 6.2 ± 0.6 bundles in controls, $n = 12$ slices, to 8.6 ± 0.9 bundles in CNT slices, $n = 13$ slices). Not only do CNT slices outgrow more β-tubulin III positive fibers but these fibers also traveled longer distances, from the edge of the outgrowing belt, displaying on average an increased (+ 31%; $P < 0.05$) length (from 450 ± 4 μm in control to 590 ± 5 μm in CNT slices, $n = 12$ and $n = 13$ slices, respectively).

In a subset of experiments (control and CNT, $n = 4$ slices), we characterized the outgrowing fibers by performing double immunostaining for the anti-β-tubulin III antibody together with the primary mouse anti-neurofilament H (SMI32) antibody (marker for projecting neurons, DRG neurons, and motoneurons).[33,37] We sampled and analyzed control ($n = 22$) and CNT ($n = 36$) slice visual fields containing distal outgrowing fibers, and we observed an overlapping between the SMI32 and the β-tubulin III signals in all ($n = 161$ and $n = 415$, control and CNT slices, respectively) thick (>10 μm) fibers detected (Supporting Figure 1). In organotypic slices, motoneurons are usually around 30/ventral horns;[34] therefore, this result indicates that MWCNTs affected even the development of neuronal processes emerging from DRGs and from other spinal projecting neurons when fibers are growing in direct contact with the substrate.[33,38]

SEM analysis of tissue cultures allowed investigating the interactions of such fibers with the carbon nanotube structure. As shown in the sample of Figure 2A1 (arrows; see also Mazzatenta *et al.*[4]), fibers appear tightly anchored to the carbon nanotube layer, with the development of membrane−substrate junctions which are never detected in fibers grown on the control surface (Figure 2A2). We next focused our attention on growth cones, at first identified by AFM. In Figure 2, panels A3 and A4 show growth cones detected in control and in CNT slices, respectively, measured at the tips of the extended neurites.

To further identify growth cones, we designed a different set of experiments, where we visualized the microtubules (by anti-β-tubulin III antibody, Figure 2B, C, in green), which are more abundant in neurite shafts and the growth cone central domain as compared to the peripheral domain. High-magnification confocal images (Figure 2B,C, control and CNT, respectively) and both bright-field and phase contrast micrographs (Figure 2D,E, control and CNT, respectively; same cultures as in B and C) show growth cones characteristically distributed at the tips and along neurites, in both control and CNT slices. Without further analyzing their morphology, we quantified the total gross number of growth cones and normalized this number to the number of the corresponding fibers (see Methods). Results are shown in the plot in Figure 2F; with respect to controls, slices cultured on the carbon nanotube substrate showed a significant increase in the normalized number of growth cones (in CNT slices, 1.40 ± 0.12 *versus* 0.9 ± 0.07 in controls, $n = 6$; $P < 0.05$).

Atomic Force Microscopy Measures of Fibers Outgrowing the Spinal Slices. We applied AFM three-dimensional imaging capability to detail the features of the outgrowing neuronal processes, focusing on fibers elongating on control or on carbon nanotube substrates. We analyzed $n = 6$ spinal slices (control and CNT), detected $n = 179$ control single fibers and $n = 263$ CNT ones, and systematically collected their width and height data values. Measurements were performed starting from high-resolution images of the basal portion of single fibers. All of the filaments crossing a region of interest, placed at about 150−200 μm from the edge of the outgrowing belt, were imaged. Neuronal outgrowing fiber width was determined starting from a linear cross section orthogonal to the fiber on which two reference cursors were placed at fiber extremes. Errors in the measurement were calculated to be on the order of ±5% of the obtained value. The fiber height was calculated as the distance between the two Gaussian distributions of substrate and fiber heights in the AFM topographic image. In the latter case, errors were computed as cumulative standard deviations.

Figure 3A shows AFM detail of neuronal fibers sprouted on a carbon nanotube substrate. Differences in color are representative of differences in height (lighter means higher). The complex morphology of the fiber is evident as well as the uniformity of the MWCNT carpet.

The height *versus* width plot in Figure 3B identifies the emergence of two populations of fibers: the control ones (open circles) and the CNT fibers (solid circles), clearly suggesting a different morphological adaptation of fibers to the carbon nanotube substrate. This is further strengthened by the distribution of the height/width ratios (HWRs) in the two populations, where the fiber cross section was idealized as a rectangular shaped area. In Figure 3C, the two distributions of the calculated HWR values are shown. Gaussian distribution fitting gives mean HWR values of 0.29 ± 0.01 and of 0.16 ± 0.01 for control and CNT neuronal outgrowing fibers, respectively. Lower values of HWR in MWCNT substrates suggest a tendency of the neuronal process to slack above the substrate, namely, with an increase in their adhesion area. Conversely, higher HWR values point to more standing fibers facing the substrate, indicating an opposite filament−surface interaction characterized by reduced relative adhesion area.

To gain insights into the mechanisms underlying the different growth potential of neuronal processes interfaced to carbon nanotubes, we used a simple AFM approach to characterize the elastic microenvironment

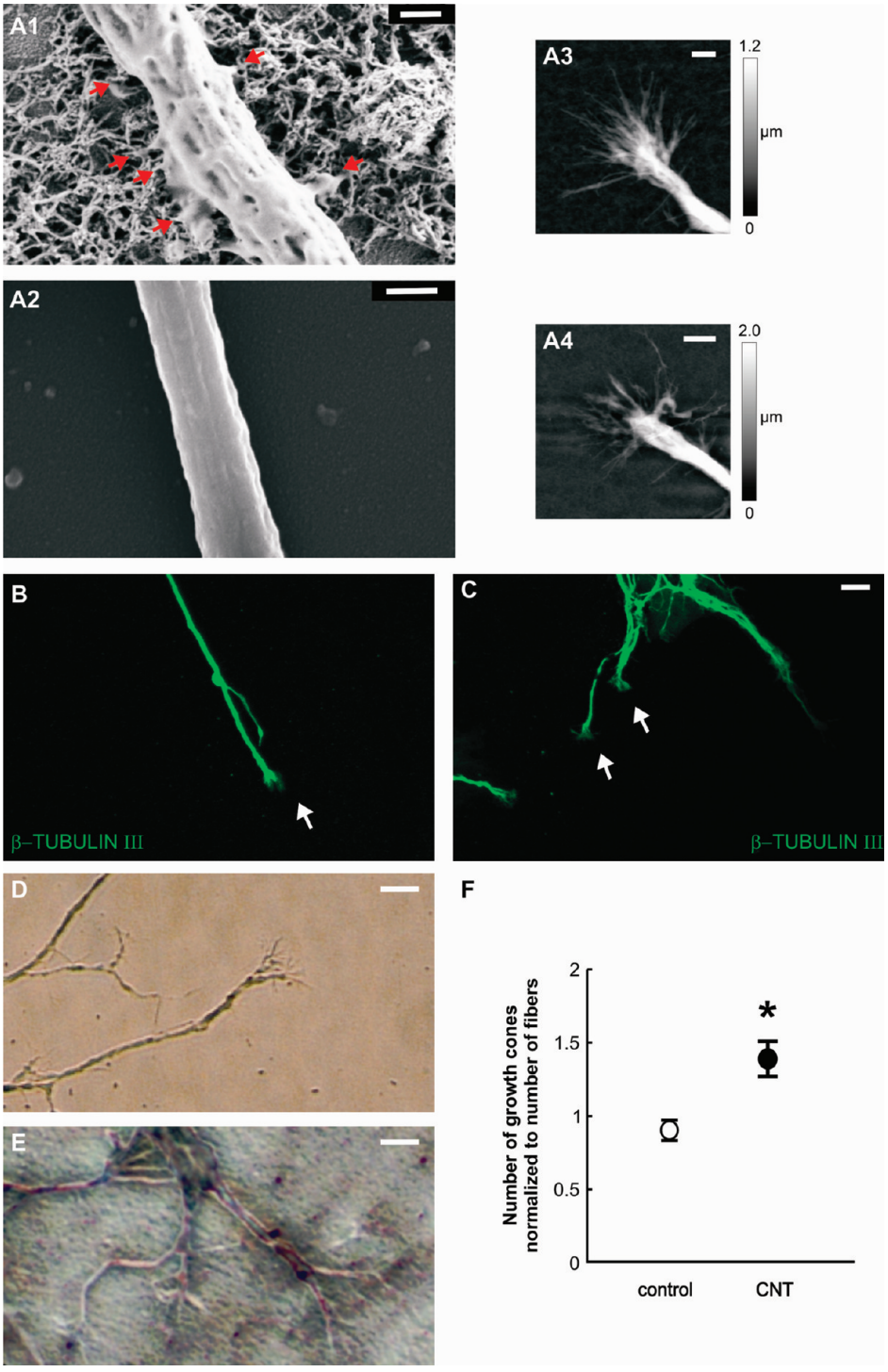

Figure 2. Spinal cord explants interfaced to MWCNTs: SEM, AFM, and confocal images of neurites and growth cones. (A1) SEM image of a spinal explant peripheral neuronal fiber on a MWCNT substrate; note the tight and intimate contacts (red arrows) between the neurite membrane and the MWCNTs. Scale bar: 500 nm. (A2) SEM image of a peripheral neuronal fiber of a control spinal explant grown on glass. Scale bar: 500 nm. (A3,A4) AFM images identify the presence of growth cones at the end of CNT (A3) and control spinal cord neurites (A4). Scale bar: 5 μm. Color scale: 0−1.2 μm in A3 and 0−2 μm in A4. (B,C) Confocal images of neuronal fibers, in control (B) and CNT (C), showing growth cones (white arrows) at the tip of β-tubulin III (in green) positive processes. Scale bar: 10 μm. (D,E) Optical microscopy images of neuronal fibers and growth cones from control spinal slices (D, bright-field image) and from CNT ones (E, phase contrast image). Same cultures as in B and C. Scale bar: 10 μm. (F) Plot quantifying the total number of identified growth cones normalized to the number of detected fibers. Note the significant increase in growth cones expressed by spinal neurites grown interfaced to MWCNTs (solid circle) as compared to control conditions (open circle; *P < 0.05). Error bar: SEM.

of neuronal branches and we quantified their relative stiffness.[39] Force spectroscopy curves were acquired starting from AFM topographic images of fiber segments on both glass and MWCNT substrates

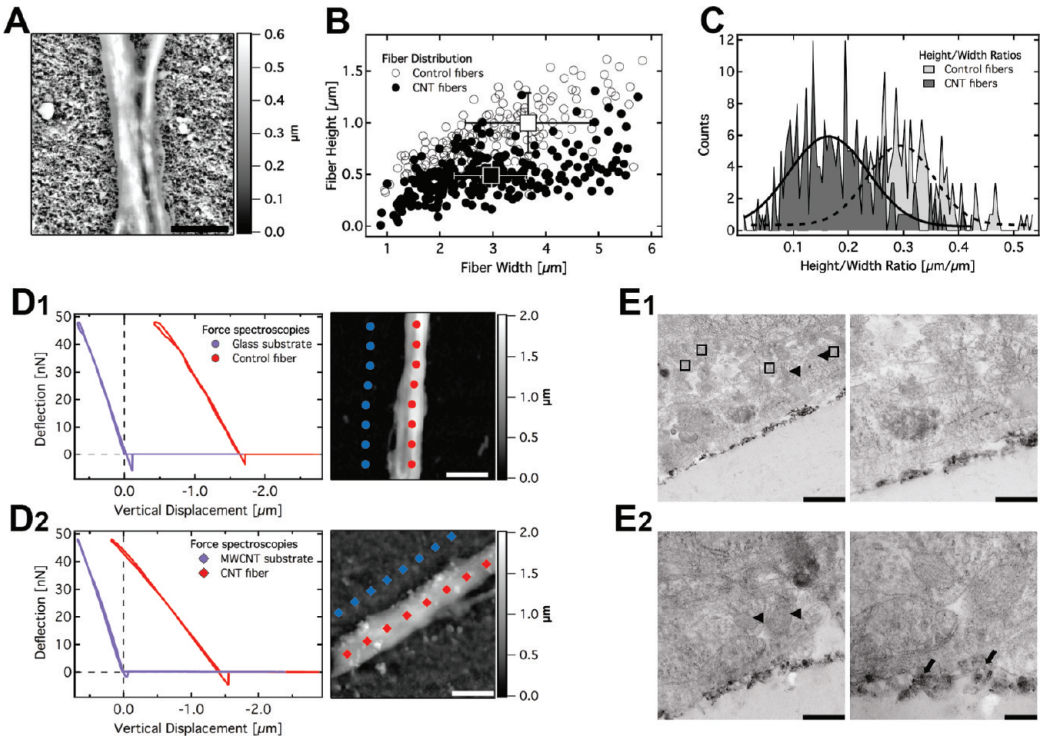

Figure 3. Morphological and mechanical characterization of spinal cord neurites *via* AFM and TEM. (A) AFM image of a neuronal process grown on a CNT scaffold. (B) Height *versus* width distribution of hypothetical rectangular cross section relative to neurites developed from control and CNT slices. Emergence of two populations of fibers is noticeable. Centers of distributions point out mean values of 1.00 μm in height and 3.66 μm in width for the fibers spread on the control substrate and of 0.49 μm in height and 2.96 μm in width for fibers on MWCNTs. Error bars: SD. (C) Same set of data is used to compute the height/width ratio (HWR) for every filament in both control and CNT cases. Note the distribution of control fibers toward higher HWR values when compared with the CNT one. (D) Force spectroscopy curves obtained from AFM images of fibers on control (D1, right) and MWCNT substrates (D2, right). Blue symbols and curves correspond to force spectroscopies performed on the substrates, and the tilted part of the plots starts at zero displacement. Red symbols and curves correspond to spectroscopies done on fibers, and the tilted part of the plots starts when the AFM tip touches the fibers. Clearly, the difference between the vertical displacements of tilt starts of the two curves corresponds to the fiber height. In this sample, control fibers appear 42% less stiff than glass substrates (42 $\pm$ 13 nN/μm for fibers *versus* a substrate of about 72 $\pm$ 1 nN/μm), while fibers on MWCNTs are 58% less stiff than carbon (30 $\pm$ 7 nN/μm for fibers *versus* a substrate of about 71 $\pm$ 2 nN/μm). (E) TEM images of sagittal sections of slices cultured (14 DIV) on MWCNTs. Note the homogeneous MWCNT carpet underlying the slice (E1) and the ultrastructural interactions between nanotubes and cell membranes (E2, right; black arrows). Note the transverse sections of neuronal fibers where microtubule sections are visible (boxes) and the presence of mitochondria (arrowheads). Scale bars: (A,D) 5 μm; (E1) 1 μm (left panel) and 500 nm (right panel); (E2) 500 nm (left panel) and 200 nm (right panel).

(Figure 3D1,D2, respectively). Such measures indicated very similar compliance values within both glass and MWCNT endowed substrates (plots in Figure 3D1,D2, left; the slope of the tilted portion of the plots, usually expressed in nN/μm, is directly proportional to surface stiffness), thus we choose to normalize to the substrate stiffness all of the data coming from different experimental sets or different tips. From this approach, it emerges that, when comparing their relative stiffness values, fiber's intrinsic elastic properties are remarkably affected by the growing substrate. In particular, CNT fibers show a significantly ($P < 0.05$) lower (−33%, from 0.70 $\pm$ 0.14 to 0.47 $\pm$ 0.03, average of normalized values; n = 6 slices) stiffness than control ones. It is tempting to speculate that this variation in fiber elastomechanical behavior is due to different fiber adaptation to the distinctive morphological and physical features of the MWCNT substrate and might also explain the apparent flattening of neurites on the carbon nanotube substrate suggested by AFM images. These observations also confirm that the measured outgrowing fibers adhere in direct contact to the substrates tested.

Transmission Electron Microscopy Visualizes the Contact Area between Carbon Nanotube and Spinal Tissue Explants. To clarify the nature and the extent of the interactions between the organotypic spinal slice and the underlying MWCNT layer, we took advantage of electron microscopy techniques. TEM studies were performed to sagittal sections of slices cultured for 14 DIV on carbon nanotubes (n = 5 slices from n = 2 culture series). Sections were analyzed to visualize the contact area between the tissue explant and the carbon nanotube carpet. As shown in Figure 3E, we documented the presence of a homogeneous MWCNT layer under the slice (demonstrating the stability of such scaffolds when deposited on culture coverslips, even after weeks of culturing).

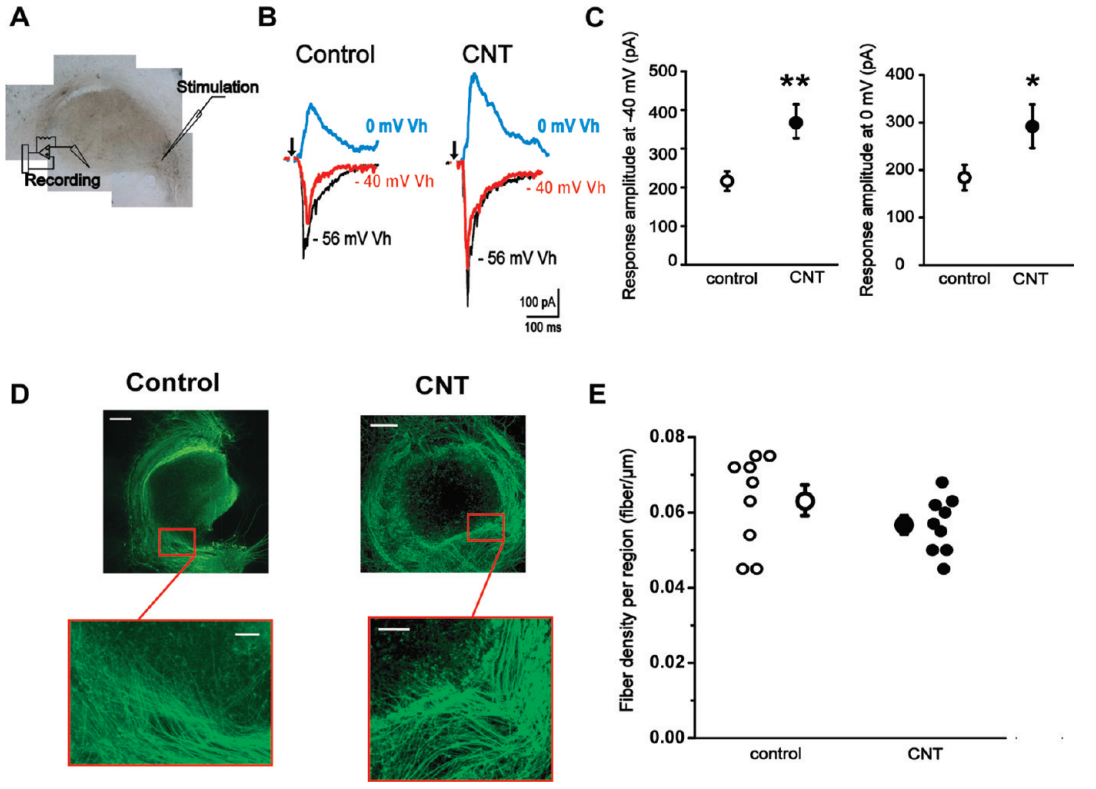

Figure 4. Evoked afferent responses of ventral spinal neurons to the electrical stimulation of the dorsal root ganglia (DRG) when interfaced to MWCNTs. (A) Schematic representation of the experimental setting. (B) Superimposed evoked postsynaptic currents (ePSCs) obtained from control (left) and CNT (right) ventral interneurons in response to DRG stimulation at the resting membrane potential (−56 mV; black), at −40 mV (red) and at 0 mV (blue). (C) Plots of the average current peak amplitude obtained from control (open circles) and CNT (solid circles) slices at −40 mV (left) and 0 mV (right) holding potentials. The peak amplitude of the PSC was significantly increased in CNT slices at both holding potentials. (D) Images of control and CNT slices, stained using the SMI32 antibody (top; scale bar: 500 μm). Bottom: enlarged views of the dorsal regions framed in top images, showing DRG fibers entering the slice (scale bar: 100 μm). (E) Plot summarizing the density of the SMI32-positive fibers entering the dorsal regions (each dot represents a dorsal region), which is similar for control (open circles) and CNT slices (solid circles). *$P < 0.05$; **$P < 0.01$. Error bar: SEM.

At higher magnification (Figure 3E1,E2, right panels), the typical TEM aspect of the MWCNTs[5] was clearly recognizable. In addition, the ultrastructural interactions between nanotubes and cell membranes (Figure 3E, right panel, arrows; see also Supporting Figure 2) in the form of tight contacts were visualized and typically displayed a discontinuous trend.[5] These observations support the hypothesis that carbon nanotube growth interfaces were directly affecting the bottom layer of the tissue explant, where, in principle, neurons could have been driven to construct a potentiated hybrid network.[5,6]

Improved Responses to Afferent Sensory Stimulations in Spinal Cord Slices Grown on Carbon Nanotube Substrates. In cultured slices, physiological neuronal connections are usually well preserved, and afferent in-growing DRG fibers establish appropriate and functional mono- or, more frequently, polysynaptic pathways toward the ventral spinal areas.[35,36] We investigated the efficacy of this incoming signaling by measuring, in control and CNT slices, polysynaptic currents elicited *via* focal electrical stimulation of the homolateral DRG (Figure 4A). Evoked postsynaptic currents (ePSCs) were heterogeneous polysynaptic responses comprising glutamate receptor-mediated and GABA-glycine receptor-mediated components.[36] In Figure 4B (black trace), mixed ePSCs are shown, elicited by DRG stimulations in control and CNT ventral interneurons held at −56 mV holding potential (V_h), a value at which all components were detected as summating inward currents. We isolated glutamate receptor-mediated and GABA-glycine receptor-mediated responses by repeating the DRG stimulations and *via* recording the ePSCs either as inward currents at V_h −40 mV (the estimated reverse value of Cl^--mediated currents; Figure 4B, red traces) or as outward currents at V_h 0 mV (the estimated reverse value of AMPA-glutamate-mediated currents, blue traces). Neurons recorded from slices grown on carbon nanotubes showed a striking 72% increase in the peak amplitude of glutamatergic ePSCs recorded at −40 mV (from 216 ± 25 pA in control slices, $n = 20$ to 371 ± 44 pA in CNT slices, $n = 24$; $P < 0.01$; plot in Figure 4C, left). No differences were detected in the ePSC delay (16.8 ± 2.6 ms in control slices; 18.1 ± 1.7 ms in CNT slices) nor in the ePSC average duration (0.22 ± 0.02 s in control slices; 0.20 ± 0.03 s in CNT slices). When recorded at 0 mV, GABA-glycine-mediated ePSCs

elicited in spinal cultures grown on carbon nanotubes showed a 59% increase in their peak amplitude (from 184 ± 27 pA, in control slices, $n = 21$, to 292 ± 46 pA, in CNT slices, $n = 20$; $P < 0.05$; plot in Figure 4C, right). Also, in this case, no differences were detected in the ePSC delay (25.0 ± 2.5 ms in control slices; 26.4 ± 2.4 ms in CNT slices) nor in the ePSC duration (0.52 ± 0.15 s in control slices; 0.48 ± 0.07 s in CNT slices).

We then explored the ePSC responses to trains (5 pulses) of DRG stimulations delivered at 5 and 10 Hz. When recorded at −40 mV, ePSCs underwent a typical frequency depression in control and CNT slices. The amplitude of the fifth ePSC was 58 ± 10% of the first one in control and 47 ± 7% of the first one in CNT slices for 5 Hz stimulation frequency (n = 12 control and 12 CNT slices), while for 10 Hz stimulation frequency, the amplitude of the fifth ePSC with respect to the first one was 53 ± 10% for control and 41 ± 9% for CNT slices (n = 11 and 10, respectively). Similar results were observed at 0 mV: for 5 Hz stimulation frequency, the amplitude of the fifth ePSC was 71 ± 5% of the first one in control and 74 ± 10% of the first one in CNT slices ($n = 9$ and 10, respectively), while for 10 Hz stimulation frequency, the amplitude ratios between the fifth and the first ePSC were 79 ± 9% for control and 59 ± 14% for CNT slices ($n = 10$ and 10 for control and CNT). These data indicated that, regardless of the potentiated ePSC responses, no alterations in the ability of ventral interneurons to integrate repetitive DRG afferent stimulations were generated by long-term coupling with MWCNTs.

Since DRG somata are typically distributed on a monolayer,[33] thus in direct contact with the MWCNT scaffold, we investigated whether the increase in evoked responses was related to an increased number of DRG fibers entering the dorsal area of the cultured slice.

We tested 4 control and 3 CNT slices. Incoming DRG fibers were visualized by SMI32 antibody (in green in Figure 4D) that has been widely used as a developmental marker for projecting neurons.[33,37]

Figure 4D (top, left and right, control and CNT slices, respectively) shows examples of labeled DRG neurons. These cells were easily recognizable and were spread out in monolayers on both sides of the slice as it has been previously described by Avossa *et al.*[33] Higher magnification fluorescence microscopy (Figure 4D, bottom left and right, control and CNT, respectively) visualizes SMI32 positive processes entering the slice dorsal area. We quantified (see Methods) the in-growing fibers analyzing 11 control and 9 CNT dorsal regions from 2 culture series (plot in Figure 4E), and we found no differences in fiber density between control (0.07 ± 0.011 fibers/μm) and CNT (0.056 ± 0.003 fibers/μm; $P = 0.19$) slices. These results suggest that, first, the DRG processes entering the slice are not increased in number, opposite to those centrifugally directed, possibly because in this case, as suggested by confocal microscopy (not shown), in-growing DRG fibers once within the dorsal area of the slice are not anymore in direct contact with the substrate. Second, the enhancement in afferent polysynaptic responses is not simply due to an increased innervation, rather other adaptive changes along the polysynaptic pathway might be involved. We cannot investigate the precise pre- and postsynaptic features along unknown polysynaptic pathways; therefore, we decided to address the spontaneous synaptic activity at the level of the ventral interneurons recorded. Spontaneous postsynaptic currents (PSCs), which are generated by action potential dependent as well as spontaneous quantal release, should mainly reflect random firing of local neurons and thus provide an index of changes in network activity.

Interfacing Spinal Explants with Carbon Nanotube Substrates Improves Spontaneous Synaptic Activity in Premotor Networks. In addition to the ability to respond to the exogenous stimulation of its afferent inputs, organotypic embryonic spinal slices display prominent spontaneous electrical activity in the ventral, premotor area.[40−42] To enable a meaningful comparison of the shifts in communication dynamics in embryonic networks developed on carbon nanotube mesh, we selected the 14 DIV stage, where neurons are known to exhibit an intense spontaneous synaptic activity.[36−42] We patch-clamped ventral interneurons (V_h −56 mV) in control (n = 65) and CNT (n = 74) slice cultures, and we recorded the emerging PSCs. In Figure 5A representative tracings are shown. In both culture groups, PSCs appeared as heterogeneous inward currents of variable amplitudes. In 12 out of 14 culture series (n = 66 neurons and n = 85 neurons, control and CNT, respectively), we observed that PSCs recorded from CNT neurons display a higher (+23%) mean current peak amplitude (from 30 ± 2 pA, $n = 66$ in control to 37 ± 2 pA, $n = 85$ in CNT; $P < 0.05$) with no differences in the PSC frequency (37 ± 1.5 Hz, $n = 66$ in control; 40 ± 1.4 Hz, $n = 85$ in CNT; $P = 0.15$).

In the large majority of spinal interneurons (both control and CNT), PSCs decayed either rapidly (τ = 2.66 ± 0.12 ms control and $\tau = 2.73 \pm 0.09$ ms in CNT) or slowly (double-exponential fitting: $\tau 1$ = 23.4 ± 3.2 ms, $\tau 2$ = 3.3 ± 0.4 ms in n = 11 control and $\tau 1$ = 23.6 ± 2.2 ms, $\tau 2 = 4.3 \pm 0.7$ ms in $n = 17$ CNT); the difference between τ values of fast-decaying PSCs and both the components ($\tau 1$, $\tau 2$) of the slow-decaying ones was statistically significant ($P < 0.001$ and $P < 0.005$, respectively) despite the similar rise times (0.8 ± 0.02 and 1.4 ± 0.04 ms, control and CNT, respectively). Figure 5B,C (left panels; superimposed tracings) shows samples of these two categories of synaptic events isolated from control and CNT neurons. In these cultures, fast (<5 ms decay time; B) events are known to represent AMPA receptor-mediated glutamate PSCs[43] while slow (>20 ms decay time; C) ones are usually due to GABA/glycine receptor-mediated ones.[36] In a

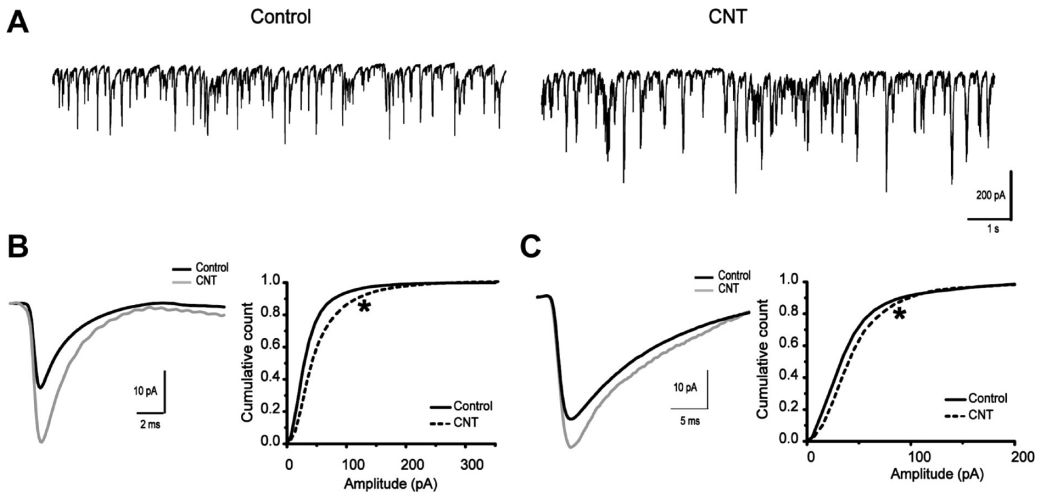

Figure 5. Spontaneous postsynaptic currents (PSCs) recorded from control and CNT ventral interneurons in spinal slices grown for 14 DIV in control or carbon nanotube substrates. (A) Representative traces of spontaneous PSCs recorded at −56 mV holding potential from one control (left) and one CNT (right) ventral interneuron. (B) Left, superimposed electronic average traces of fast-decaying synaptic events from control (black) and CNT (gray) neurons (same cells as in A); right, cumulative distributions of fast PSCs amplitudes (n = 14 cells in control and n = 25 cells in CNT slices). (C) Left, superimposed electronic average traces of slow-decaying synaptic events from control (black) and CNT (gray) neurons (same cells as in A); right, cumulative distributions of slow PSCs amplitudes (n = 12 cells in control and n = 18 cells in CNT slices). *P < 0.001.

simplified manner, this off line procedure allowed us to isolate the two major components of these immature networks[36] avoiding any interference with the spontaneous synaptic drive to recorded interneurons brought about by the use of pharmacological tools or by changes in the cell holding potential. In our recordings, in CNT neurons, both fast and slow events displayed an increased amplitude even when separately analyzed, as shown in the cumulative plots of Figure 5B,C (right panels), where peak PSC amplitudes for controls were distributed to the left of CNT ones (the two curves were significantly different in both cases; P < 0.001). Apparently the potentiation, due to carbon substrates, of fast synaptic components was stronger relative to that of slower ones. These observations are intriguing; in fact, none of the recorded neurons was in direct contact with carbon nanotube layers, known to potentiate neuronal signaling and synapses when MWCNT/neuronal network hybrids are formed on a monolayer.[5,6] On the contrary, only the bottom layer of the slice explant (14 DIV slices comprise 4−5 layers of cells; see Methods) is positioned in direct contact with the MWCNTs (shown by TEM in Figure 3E).

We also asked whether changes in the local excitatory synaptic connectivity (for example, the number of functional presynaptic boutons) of ventral interneurons, which are not in direct contact with the MWCNT scaffold, were present. Single-neuron voltage-clamp recordings of spontaneous synaptic activity were performed in the presence of 1 μM tetrodotoxin (TTX) at 14 DIV. TTX is a well-known voltage gated, fast Na^+ channel blocker that inhibits action potentials. Thus, spontaneous events recorded in the presence of TTX, termed miniature PSCs, rely on the action potential-independent stochastic fusion of neurotransmitter vesicles at the presynaptic membrane, and their frequency is traditionally accepted to be proportional to the number of synaptic contacts.[44] We recorded pharmacologically isolated miniature excitatory postsynaptic currents (mEPSCs) in the presence of strychnine (1 μM, to block glycine receptors)[36] and bicuculline (10 μM, to block $GABA_A$ receptors)[36] from control and CNT slices. Both amplitude and frequency of mEPSCs were similar in the two culturing conditions (19.4 ± 1.5 pA, n = 15 in control, 19.8 ± 1.5 pA, n = 27 in CNT slices; 11.5 ± 2.9 Hz, n = 15 in control, 8.2 ± 1.3 Hz, n = 27 in CNT slices; see Supporting Figure 3).

In summary, our electrophysiological findings suggest that remote alterations in synaptic connectivity and/or firing activity, possibly at the layer of neurons in direct contact to MWCNTs,[6] are affecting the ability of excitatory inputs (elicited by stimulation or emerging spontaneously) to synchronize either the network, leading to larger polysynaptic responses, or the synaptic boutons, leading to larger postsynaptic currents. The mechanisms that underlie these effects are not easy to tackle. Our data do not support the presence of local changes in the number of presynaptic release sites or in other pre- and postsynaptic features of the recorded interneuron and do not support a local increase in firing activity (the frequency of PSCs is never increased), but we cannot exclude the presence of activity-dependent forms of plasticity underlying the amplification of the signals detected at the level of the ventral cells. To clarify these issues, further studies will be necessary; in particular, it will be instrumental to include computer simulations to model network interactions between potentiated neurons connected *via* carbon nanotubes and nonpotentiated neurons connected *via* synapses. Additionally,

unknown second messenger pathways, generated at the carbon nanotube/neuron interface, may be transported and act along axons and synapses.

We cannot entirely exclude that the effects on remote neurons are mediated by small amounts of detached MWCNTs, internalized by cells within the spinal explants, and not detected by our routine TEM analysis; however, some observations seem to rule out this possibility. In fact, in a previous study, we showed that internalization of MWCNT *per se* did not affect synaptic activity in cultured hippocampal neurons.[45] We further tested this hypothesis here, by incubating organotypic slices with MWCNTs (1 μg mL^{-1}) for 6 days, in the absence of MWCNTs at the interface (*i.e.*, cultured on control coverslips). Such a concentration mimics a 10% detachment from the MWCNT layer. Mixed PSCs recorded from neurons in MWCNT-treated cultures did not display an increase of their peak amplitudes with respect to controls (not shown; on average 26 $\pm$ 3 pA, n = 10 in control *vs* 22 $\pm$ 2 pA, n = 10 cells in MWCNT-incubated cultures; P = 0.084). However, we wish to outline that the biological effects of soluble carbon nanotubes can be highly variable depending on several issues, including the approaches used to render carbon nanotubes water-soluble.[46]

Taken together, our results are promising in that they demonstrate the presence of remote MWCNT effects on neuronal networks, never described before.

CONCLUSIONS

The results presented here expand our knowledge of the interactions between carbon nanotubes and neurons. Our multidisciplinary approach reveals for the first time that the long-term impact of an artificial MWCNT meshwork characterized by large surface roughness and conductivity[5,6] favors neurite regrowth in spinal explants with the appearance of increased growth cone activity. We speculate that these effects may be, at least in part, mediated by direct interactions among nerve fibers and MWCNTs, used as an exoskeleton and climbed *via* formation of membrane/material tight junctions. Indeed, our TEM measurements document membrane interactions as previously described in simplified neuronal networks[5,47] or by SEM[9] or, by AFM, in lipid bilayers.[48] Such interactions may influence, for example, mechanical forces modulating adhesion processes, as suggested by our AFM measurements.

These findings sustain the exploitation of mechanical properties in tissue engineering scaffolds, able to promote nerve fiber elongation. Mechanically defined microenvironments may effectively be transduced into biochemical signaling relevant to CNS reconstruction. Ultimately, our study supports one of the emerging strategies in nanoscale engineering: the use of physical features alone to guide different biological responses, without the levels of sophistication required by biomolecule selective patterning.[18,19]

Finally, for the first time, we explored an additional issue: how far carbon nanotube-mediated potentiation of neuronal signaling[5,6,28] is sensed in synaptic networks remote from the MWCNT interface, under chronic conditions. Noteworthy, after weeks of MWCNT interfacing, neurons located at as far as 5 cell layers from the substrate display an increased efficacy in synaptic responses (which could represent either an improvement or a pathological behavior), presumably mediated by ongoing plasticity driven by the neuron/carbon nanotube hybrids.[5] Intriguingly, the overall ability of premotor networks to process information is conserved when tested with incoming high-frequency inputs.

The development of nanomaterial-based interfaces for neuronal networks holds the potential to improve our knowledge on the adhesive interactions that cells and fibers are able to probe and respond to. In addition, nanomaterial-based scaffolds allows one to investigate the ability of multilayered nervous tissue in translating adhesive interactions into network activity in regions relatively far from the interface itself, providing relevant information for the scientific community dealing with neuronal interfaces and carbon nanotubes. Ultimately, hybrids able to boost synaptic performance may be exploited to test information processing in neuronal networks.

Engineered nanomaterials provide new and exciting opportunities to improve materials and to design new products with high benefit potentials, but at the same time, their unique physicochemical properties pose potential risks to the health of humans. Carbon nanotubes, in particular, are currently at the center of a strong debate regarding their safety and use. An increasing amount of evidence indicates that carbon nanotube toxicity/pharmacodynamics is critically influenced by the route of exposure/administration and, importantly, by their functionalizations.[49] Future developments of scaffolds/devices based on the carbon nanotube technology will therefore need to take into account these issues. We have also to consider that currently several studies report the use of functionalized carbon nanotubes in soluble forms for neurological applications.[50,51] The future design of carbon nanotube-based technologies will therefore have to guarantee their stability and, consequently, full biocompatibility and safety.

METHODS

Substrates and Culture Preparation. MWCNT-coated substrates were prepared following our previous work based on the 1,3-dipolar cycloaddition[5,6] (optimized MWCNT solution concentration 0.01 mg/mL; final MWCNT film density 7 $\times$ 10^{-5} mg/mm^2). Briefly, 20−30 nm MWCNTs (Nanostructured & Amorphous

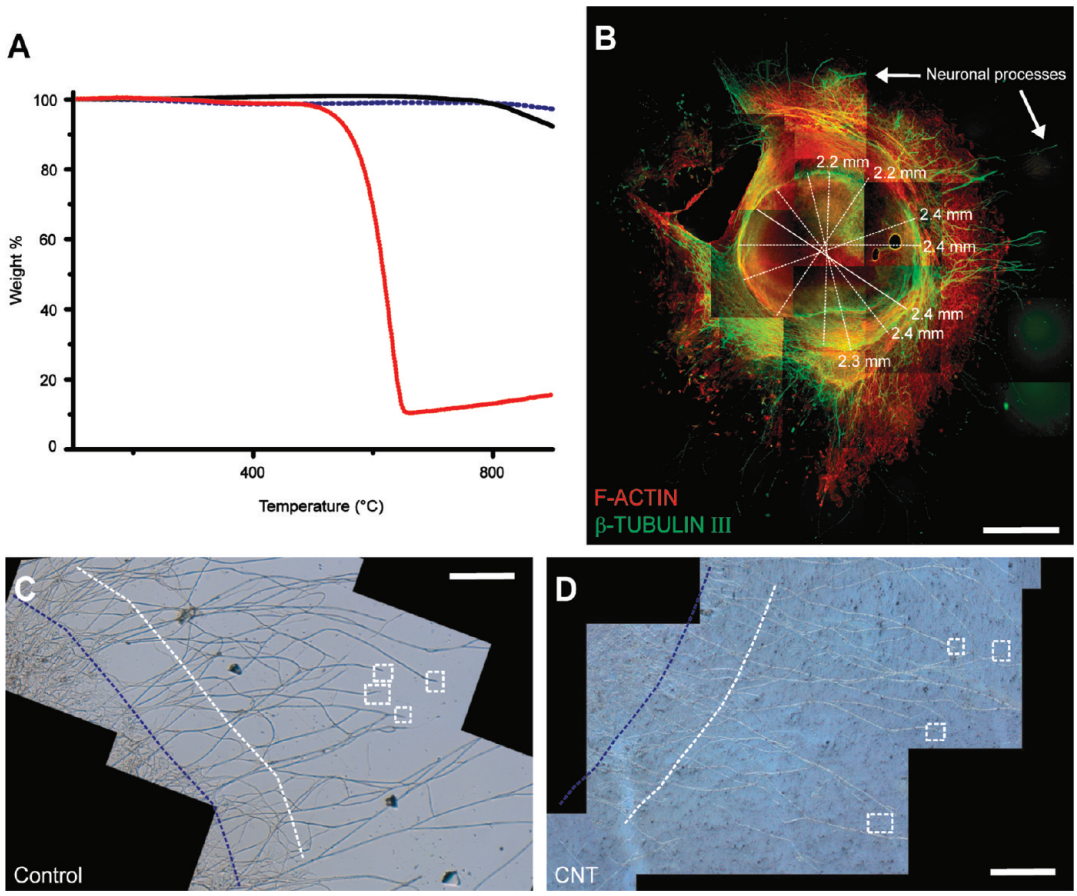

Figure 6. MWCNT TGA assessment and cultured slice morphology. (A) Thermogravimetric analysis (TGA) under nitrogen (dashed blue and black) and under air (dotted red). Inert atmosphere (nitrogen) TGA analysis provides information about the degree of MWCNT functionalization: the loss of weight determined at 400 °C (dashed blue) is correlated with the amount of functional groups per gram of material through the molecular weight of the organic moiety bound to MWCNTs. The calculated degree of functionalization is 0.1 mmol/g. After MWCNT exposure at 350 °C under N_2 for 20 min, a complete repristinization of MWCNTs is obtained (black). TGA run in the presence of oxygen measures the metal content of MWCNTs (dotted red). Metallic residue in the sample is as low as 10%. (B) Immunofluorescence of 8 DIV spinal slice with F-actin (red) and β-tubulin III (green) positive cytoskeleton components. The original spinal explant, without the DRG and outgrowth area, is the almost circular region located at the center. The outgrowth belt surrounding the slice is composed of a dense actin network presumably belonging to both neuronal and non-neuronal cells, usually coexplanted with the tissue. Neuronal processes (white arrows) can be clearly observed when emerging from this belt of dense actin network. Scale bar: 1 mm. (C,D) Images showing a small region of slice cultured on glass (C) and on CNT substrate (D). The blue dashed line in C and D indicates the boundary of the belt, while the white dashed line indicates the 150−200 μm distance from the boundary, where the number of neuronal process was quantified. The white boxes indicate growth cones. Scale bar: 200 μm.

Materials, Inc.), used as received, were functionalized using 1,3-dipolar cycloaddition with heptanal and sarcosine at 130 °C for 120 h in dimethylformamide (DMF) as solvent, as previously described.[28] TGA (plot in Figure 6A) was performed using a Q500 (TA Instruments) to characterize functionalized MWCNTs, and TGA analyses under N_2 or under air were recorded, by equilibrating at 100 °C and following a ramp of 10 °C/min up to 1000 °C. In the case of defunctionalized MWCNTs, the material was analyzed after 20 min exposure to high temperature (350 °C) under N_2.

Once the material was characterized, a DMF solution of functionalized MWCNTs (0.01 mg/mL) was deposited and left to evaporate at 80 °C, then the substrates were heated at 350 °C under N_2 atmosphere to induce the complete repristinization of MWCNTs. Paraffin (Parafilm, Pechiney Plastic Packaging) molds were used to circumscribe an area of 110 mm^2 located at the center of the glass coverslips where the MWCNTs were deposited, corresponding to the area where the slice explants were positioned. Paraffin molds were removed prior to heating.

Soluble MWCNTs were obtained through a 1,3-dipolar cycloaddition reaction, introducing N-substituted pyrrolidinic rings with amino-terminated ethylene glycol solubilizing chains. The amount of functional group was determined by quantitative Kaiser test and corresponds to 133 μmol g^{-1}.

Organotypic slice cultures of spinal cord and DRG were obtained from mouse embryos (F1 hybrid C57BL6xSJL) at embryonic day (E) 12−13, as previously described.[33,42,52] Briefly, the fetuses were obtained by cesarean delivery from timed-pregnant mice sacrificed by cervical dislocation (a procedure in accordance with the regulations of the Italian Animal Welfare Act, with the relevant European Union legislation and guidelines on the ethical use of animals, and approved by the local Authority Veterinary Service). Fetuses were then decapitated, and their backs from low thoracic and high lumbar levels were isolated and cut into 275 μm thick transverse slices. Each spinal cord slice (with its DRG) was then fixed on a glass coverslip (named control) or on a MWCNT-covered coverslip (named CNT slice) with chicken plasma (Rockland) clotted with thrombin (Sigma). The coverslips were inserted into plastic tubes with 1 mL of medium containing 67% DMEM (Invitrogen), 8% sterile water for tissue culture (Invitrogen), 25% fetal bovine serum (Invitrogen), and 25 ng/mL nerve growth factor (Alomone Laboratories); osmolarity, 300 mOsm; pH 7.35. The tubes were kept in a roller drum rotating 120 times per hour in an incubator

at 37 °C in the presence of humidified atmosphere, with 5.2% CO_2. Slices were kept in culture for 8−21 days.

Immunofluorescence. Organotypic cultures (control and CNT, 8−10 DIV) were fixed with 4% paraformaldehyde (PFA) in PBS for 1 h at room temperature (RT), washed in PBS, and incubated at 37 °C for 30 min in blocking solution consisting of 5% FBS and 0.3% Triton-X 100 in PBS. Upon washing (in PBS), fixed slices were incubated for 2 h at 37 °C with primary antibodies: mouse monoclonal anti-GFAP (Sigma G3893, 1:200 dilution) and rabbit polyclonal anti-β-tubulin III (Sigma T2200, 1:250 dilution). After the primary incubation and PBS wash, slices were incubated for 2 h at 37 °C with Alexa 594 phalloidin in order to highlight F-actin (Invitrogen A12381, 1:100 dilution), Alexa 488 goat anti-mouse (Invitrogen A10667, 1:500 dilution), and Atto 633 goat anti-rabbit (Sigma 41176, 1:500 dilution) against mouse GFAP and rabbit β-tubulin III, respectively.

For the double staining for neurofilament H and β-tubulin III, slices were incubated with the primary mouse anti-neurofilament H (SMI32) antibody[33,37] (Sternberger Monoclonals Inc.; 1:200) and the rabbit polyclonal anti-β-tubulin III one (Sigma T2200, 1:250), overnight at 4 °C. After being washed with PBS, slices were incubated for 2 h at 37 °C with the secondary antibodies Alexa 488 goat anti-mouse (Invitrogen A10667, 1:250) and Alexa 594 goat anti-rabbit (Invitrogen A12381, 1:250). Slices were imaged at 20× magnification using a fluorescent microscope (Leica DMLS, Wetzlar, Germany). The analysis was performed using the ImageJ software (http://rsbweb.nih.gov/ij/).

To estimate the number of cell layers, we performed nuclear staining by incubating the slices at 14 DIV with the nucleic acid binding fluorescent dye TO-PRO-3 (Molecular Probes; 1:500 dilution, final concentration 2 μM) for 1 h.

Image Acquisition and Confocal Microscopy. Upon immunofluorescence staining, organotypic spinal slices were imaged using either a fluorescent microscope (Leica DMLS, Wetzlar, Germany) or a confocal microscope (Nikon Eclipse C1si, equipped with Ar/Kr and He/Ne lasers). The entire slice was imaged at 10× magnification. In the case of confocal images, sections were acquired at different focal planes every 1.5−2 μm and the total stack thickness was approximately 12−15 μm.

Reconstructions of the slice images were performed offline using the image processing package Fiji (http://fiji.sc/wiki/index.php/Fiji). For the confocal stack of images, the *z* projection of the stack was obtained prior to reconstruction. The analyses were then performed using the ImageJ software (http://rsbweb.nih.gov/ij/). Figure 6B illustrates a sample of an organotypic slice (8 DIV) co-labeled for F-actin (in red) and β-tubulin III (in green). To quantify slice dimensions, we measured at 8 DIV the diameter of the spinal area corresponding to the initial tissue explant (excluding DRGs and fiber outgrowths) in control and CNT cultures. In each slice, we measured 10 times at different orientations the distance between opposite edges of the slice and then averaged the obtained values (see dashed lines in Figure 6B). On average, control (n = 12) and CNT (n = 13) slices did not differ in terms of explanted tissue diameter, which was around 2.60 mm in all cultures analyzed.

To quantify the number of neuronal processes exiting the spinal tissue, we decided to select those crossing the edge of the growing belt (dashed blue lines in Figure 6C,D) surrounding the cultured slices, whose complexity in terms of growing mesh of fibers prevents clear identification of β-tubulin III positive processes. In our analysis, we opted to routinely select and quantify, using reconstructed images, the thicker fibers (>10 μm) presumably representing bundles of fibers, exiting the growing belt of at least 150−200 μm (dashed white lines in Figure 6C,D). By estimating only thick fibers, we presumably underestimated the real number of single neuronal processes. In fact, at the used magnification, the presence of immunofluorescent bundles of fibers prevents a clear-cut identification of single fibers since multiple strands of individual β-tubulin III positive neuronal processes are very close to each other. The length of the detected thick fiber was estimated as the linear distance between the point in which it emerges from the edge of growth belt and its visible tip (samples are shown in Figure 6C,D, control and CNT slices, respectively).

At higher magnification (60×) by confocal analysis, a single neurite could be identified and corresponded to a single thin (<5 μm) and long β-tubulin III positive neuronal process emerging from the growth belt. Single fibers were further analyzed by AFM (see below).

High-magnification optical images were used in order to evaluate the number of growth cones. First, we acquired the entire image, where we morphologically identified the area of interest and neurites, such as those represented in Figure 6C,D (neurite tips are highlighted by the white boxes).

At higher magnification growth cones were subsequently quantified (see results and Figure 2D−F). In order to standardize our measurements, the total number of growth cones thus identified was normalized to the number of detected neurites, with a ratio of 1 when every neuronal fiber ends in a single identifiable growth cone; <1 when some of the detected neurite does not show a clear identifiable growth cone; >1 when more growth cones are detected at the tip and along a single neurite.

To quantify the number of DRG processes entering the slice dorsal area, we stained slices with the anti-neurofilament H SMI32 antibody (Sternberger Monoclonals Inc.). We then identified the two dorsal quadrants in each slice. We quantified all of the SMI32 positive fibers crossing a 600 μm long line tangential to the edge of the slice in 2−4 dorsal regions per slice.

The microscopic structure of the organotypic slice cultures used for the present study was investigated to establish the approximate degree of multilayer organization. When the slice was viewed with a confocal microscope after immunostaining with the nuclear acid specific dye TO-PRO-3, we measured, in 14 DIV slices, 4−5 cell layers, while the DRG cells were organized as a monolayer. TO-PRO-3 fluorescence was detected by a confocal microscope (Nikon Eclipse C1si, equipped with Ar/Kr and He/Ne lasers). Three different regions of interest were identified in three different slice culture series, and the entire thickness of each region was imaged to obtain a *Z*-stack with sections at an interval of 0.3 μm. ImageJ software was used to analyze the peak of cell nuclei fluorescence, allowing the layer organization of each region of the slice to be determined. The number of cell layers present in a slice is taken as the average of the number of nuclei layers detected in all of the regions sampled.

Transmission Electron Microscopy and Scanning Electron Microscopy. TEM visualization of MWCNTs was performed on a Philips EM 208 TEM, using an accelerating voltage of 100 kV. About 1 mg of compound was dispersed in 1 mL of DMF. Then, one drop of this solution was deposited on a TEM grid (200 mesh, nickel, carbon only). By TEM analysis, we confirmed that dispersed MWCNTs displayed a diameter within the 15−20 nm range and an average length around 500 nm.[6]

For TEM analysis, organotypic slice cultures at 14 DIV were washed with 0.1 M cacodylate buffer (pH = 7.2) and fixed with a solution containing 2% glutaraldehyde (Fluka, Italy) in 0.1 M cacodylate buffer for 1 h at RT. Cultures were then washed in cacodylate buffer and then transferred into a cacodylate buffer solution containing 1% osmium tetroxide (Fluka) for 1 h at 4 °C. After further wash with cacodylate buffer, cultures were dehydrated. Propylene oxide was used to wash the samples, which were then embedded in a mixture of propylene oxide and epoxy resin (DER 332-732 Electron Microscopy Sciences) and placed in the oven for 1 h at 37 °C. This mixture was then removed and substituted with epoxy resin (DER 332-732) for 1 h at 45 °C. Then the resin was renewed and stabilized for 1 h at 37 °C, and eventually a final refresh of new resin was performed for 24 h at 37 °C (infiltration), for 24 h at 45 °C (reticulation), and for 24 h at 60 °C (inclusion/solidification). For routine block check-outs, 0.5−2 μm thick semithin sections were stained with 1% toluidine blue (Sigma) plus 1% disodium tetraborate (Sigma) in water. Ultrathin sections (100 nm) were obtained by cutting the samples in a plane sagittal with respect to the surface. Sections were then collected onto 200 and 300 mesh nickel or copper grids and stained with uranyl acetate (2% in water) and lead citrate (Fluka). TEM analysis was performed on 10 ultrathin sections from two culture series (total 5 organotypic slices). TEM measurement was also performed on CNT cultures to assess the presence of abnormalities. We never observed obvious disperse

or scattered MWCNTs in the slice core or within intracellular domains.

SEM measurements were carried out with a Zeiss Supra microscope on 8 DIV cultured slices (control and CNT) fixed as for TEM analysis and then dehydrated in absolute ethanol. Images were acquired collecting secondary electrons on a commercial SEM (Gemini SUPRA 40, Carl Zeiss NTS GmbH, Oberkochen). In order to prevent electron-induced surface charging, low accelerating voltages (0.6−1.0 keV) were used for slice visualization. Slices grown on CNTs were imaged without any prior metallization process, while those grown on glass were metallized prior to SEM imaging with a thin Pt/Pd film.

Atomic Force Microscopy. AFM was used in the present work to acquire three-dimensional images of representative cultured slice constituents. In control and CNT samples (fixed at 8−10 DIV and dehydrated as for SEM analysis), single fibers were imaged *via* AFM in order to characterize their height relative to the supporting substrate. Precise planar measurements were possible together with unambiguous height measurements. All AFM images were acquired using a commercially available microscope (MFP-3D Stand Alone AFM from Asylum Research, Santa Barbara, CA) endowed with a 90 μm × 90 μm × 15 μm closed-loop metrological scanner. Measurements were carried out in air at room temperature working in dynamic mode. Cantilevers, characterized by a resonant frequency of about 174 kHz (NSG11/B tips from NT-MDT Co., Moscow, Russia), were used working at low oscillation amplitudes with half free amplitude set-point. High-resolution images (1024 × 1024 pixels frames) were acquired at 0.75 lines/s scan speed. Slide branch height was characterized starting from sequences of transversal stripe images (1024 × 64 pixels) crossing all of the filaments intersecting a region of interest (ROI) placed at about 150−200 μm from the slice outgrowth belt (Figure 6C,D).

AFM elastic assessment of stiffness was done taking advantage of the distinctive force spectroscopy capabilities of the MFP-3D AFM. In brief, force spectroscopy measures the deflection of an AFM cantilever while it is pushed to a surface. Deflection can then be interpreted as tip−surface applied force *via* cantilever spring constant and displacement knowledge.

Compliance of the material under the tip may be determined and thus stiffness ratios between the different materials or cellular elements composing the surface under investigation.[39,53,54]

Eight DIV cultured slices on control glass and CNT-loaded substrates were analyzed in air at room temperature after fixation and dehydration in absolute ethanol.

Measurements were done on fibers belonging to the same ROI of the previous AFM morphological characterization. After the identification *via* AFM imaging of a portion of the fiber lying down on glass or carbon nanotubes, a series of 8 punctual force spectroscopy curves were performed on both the fiber body and the neighboring substrate area (Figure 3D1,D2). Average of the two series of 8 curves was computed and used to compare fiber/substrate mechanical properties. Indication of material compliance comes from the slope of the tilted part of force spectroscopy plots (Figure 3D1,D2, respectively for glass and CNT substrates). On the basis of the fact that MWCNT substrates when compared to control substrates show similar (96 ± 2%) values in terms of stiffness, all data coming from different sets of experiments or from different batches of AFM tips were normalized to substrate stiffness values. Cantilever used was a 40 nm tip radius probe characterized by a spring constant of about 0.12 nN/nm (CSC21/Ti−Pt tips from MikroMasch Co., Tallinn, Estonia). Force spectroscopy measurements were performed at constant speed (1 μm/s) and include both an extension and retracting branch. Substrate stiffness is directly correlated with the slope of force plot tilted part (higher gradient means higher substrate stiffness). Measurement starts moving the tip of about 3 μm far from the substrate surface to start the approach branch of the curve (horizontal portion of the force plots). When the tip touches the surface, it starts to bend and the force plot tilts (taking heed of the cantilever elastic constant) proportionally with surface stiffness.[54] We set a trigger point to start tip retraction from the surface when the applied force reaches a value of about 50 nN. At this point, the tip retracts, moving in opposite direction, until the surface contact is loose and moves again to the starting point, ready for a new force spectroscopy cycle.

Regarding force measurements, average values of 8 force curves acquired on the fiber and of an equal number on the relative substrate were considered. Following this approach, we acquired 10 sensible values of stiffness for at least 3 fibers per slice sample. Three couples of slices, control and MWCNT surfaces, were mechanically characterized *via* force spectroscopy. All stiffness measurements have to be considered as relative ones, meaning we were interested in comparing fiber stiffness relatively to the supporting substrate to point out substrate-induced changes in the fiber mechanical response. Particular effort was done in choosing fibers with comparable shapes in terms of width, height, and absence of immediate branching in proximity of the fiber chop. No attempts of absolute determination of fiber stiffness were done in this work.

Gwyddion software (www.gwyddion.net) was used to analyze all AFM images while all statistics and data processing were performed using Igor Pro software (www.wavematrics.com).

Electrophysiological Recordings. Whole-cell patch-clamp recordings in the voltage clamp mode were performed on slices at 13−21 DIV at RT. For each experiment, a coverslip with the spinal culture was positioned in a recording chamber, mounted on an inverted microscope, and superfused with normal Krebs' solution containing (in mM): 152 NaCl, 4 KCl, 1 $MgCl_2$, 2 $CaCl_2$, 10 HEPES, and 10 glucose. The pH was adjusted to 7.4 with NaOH. Recordings were obtained from visually identified neurons (see below) with pipettes (4−6 MΩ) filled with a solution of the following composition (in mM): 120 K gluconate, 20 KCl, 10 HEPES, 10 EGTA, 2 $MgCl_2$, 2 Na_2ATP. The pH was adjusted to 7.3 with KOH. The uncompensated value for series resistance was 8−10 MΩ; previous experiments have shown that these experimental conditions enabled recordings of synaptic currents without significant distortion.[36,55] Voltage values indicated in the text are not corrected for the liquid junction potential, estimated around 13 mV.

Recordings were performed on visually identified ventral interneurons. In accordance with previous investigations, neurons were termed interneurons when their cell body diameter was between 10 and 20 μm, making them clearly distinguishable from motoneurons (30−60 μm diameter, generating long processes) and from DRG neurons (40 μm diameter, with just one or two large processes emanating from it).[33,38,42] Electrophysiological responses were amplified (Axopatch 1-D, Axon Instruments, and EPC-7, HEKA), sampled and digitized at 10 kHz with the pCLAMP software (Axon Instruments) for off-line analysis.

Patch clamped interneurons from controls and CNT slices displayed similar passive properties (input resistance: 365 ± 29 MΩ in control, 314 ± 24 MΩ in CNT; cell capacitance 95 ± 5 pF in control, 98 ± 6 pF in CNT; $n = 61$ and $n = 78$, control and CNT, respectively).

Bipolar electrodes made by a low-resistance patch pipet containing normal Krebs solution were used to deliver the extracellular electrical stimulations to the DRG ipsilateral to the patched interneurons. Short voltage pulses (200 μs) of variable amplitude (1−50 V) were delivered by a Digitimer DS2 stimulator every 40 s (an interval allowing reproducible responses; not shown) or as trains of 5 pulses at 5−10 Hz.

In each experiment, voltage pulses of increasing amplitude were delivered to the DRG and a stimulation intensity/response current amplitude curve was constructed; the response to a stimulation intensity eliciting 80% of the maximal response was then used for the comparison between the different experiments. In our experiments, a monosynaptic component, identified by the short delay (<5 ms), in the response to DRG stimulation was observed in only a minority (<15%; $n = 58$ control and CNT) of cases, and therefore, these responses were excluded from the analysis.

Each ePSC is the average of 5−10 consecutive stimulations. The amount of depression for the responses to trains of 5 DRG stimulations delivered at 5 or 10 Hz was assessed by comparing the amplitude of the responses obtained to the fifth pulse in the train to that of the first one.

Single spontaneous synaptic events were detected by use of the AxoGraph X (Axograph Scientific) event detection

program on an Apple Computer workstation.[56] On average, 2000 PSCs were analyzed from each cell in order to obtain mean kinetic and amplitude parameters. From the average of these events, we measured the rise time, calculated from 10 to 90% peak amplitude, the peak amplitude and the value of decay (expressed as τ) by fitting a monoexponential (for AMPA-mediated events) or biexponential (for GABA-mediated events) function.

Miniature excitatory postsynaptic currents (mEPSCs) were recorded at −70 mV holding potential to increase the driving force for the excitatory currents, in the presence of TTX (1 μM; Latoxan), strychnine (1 μM; Sigma), and bicuculline (10 μM; Tocris). mEPSCs were analyzed by the Clampfit 10 software (pClamp suite, Axon Instruments). On average, 200−500 mEPSCs were analyzed from each cell.

Data Analysis and Statistics. Results are presented as mean ± SEM; *n* is the number of neurons, if not otherwise indicated. Statistically significant difference between two data sets was assessed by Student's *t* test (after validation of variances homogeneity by Levene's test) for parametric data and by Mann−Whitney for non-parametric ones, while data distributions (see cumulative distributions in the Results section) were compared by the Kolmogorov−Smirnov test.

Conflict of Interest: The authors declare no competing financial interest.

Acknowledgment. We acknowledge D. Avossa for the reconstruction of organotypic culture reported in Figure 4C, C. Gamboz for TEM. The TASC national laboratory (Trieste) is also gratefully acknowledged for SEM assistance. We are indebted to M. Grandolfo for her help with TEM data, histology protocols, and critical comments, and to L. Masten for culturing procedures. Financial support from ERC grant CARBONANO-BRIDGE No. 227135 is gratefully acknowledged. Financial support from ERC grant CARBONANO-1076 BRIDGE No. 227135 and that from the Italian Ministry of Education MIUR (cofin Prot. 20085M27SS) are gratefully acknowledged.

Supporting Information Available: Supplemental results. This material is available free of charge *via* the Internet at http://pubs.acs.org.

REFERENCES AND NOTES

1. Patolsky, F.; Timko, B. P.; Yu, G.; Fang, Y.; Greytak, A. B.; Zheng, G.; Lieber, C. M. Detection, Stimulation, and Inhibition of Neuronal Signals with High-Density Nanowire Transistor Arrays. *Science* **2006**, *313*, 1100–1104.
2. Silva, G. A. Neuroscience Nanotechnology: Progress, Opportunities and Challenges. *Nat. Rev. Neurosci.* **2006**, *7*, 65–74.
3. Galvan-Garcia, P.; Keefer, E. W.; Yang, F.; Zhang, M.; Fang, S.; Zakhidov, A. A.; Baughman, R. H.; Romero, M. I. Robust Cell Migration and Neuronal Growth on Pristine Carbon Nanotube Sheets and Yarns. *J. Biomater. Sci. Polym. Ed.* **2007**, *18*, 1245–1261.
4. Mazzatenta, A.; Giugliano, M.; Campidelli, S.; Gambazzi, L.; Businaro, L.; Markram, H.; Prato, M.; Ballerini, L. Interfacing Neurons with Carbon Nanotubes: Electrical Signal Transfer and Synaptic Stimulation in Cultured Brain Circuits. *J. Neurosci.* **2007**, *27*, 6931–6936.
5. Cellot, G.; Cilia, E.; Cipollone, S.; Rancic, V.; Sucapane, A.; Giordani, S.; Gambazzi, L.; Markram, H.; Grandolfo, M.; Scaini, D.; *et al.* Carbon Nanotubes Might Improve Neuronal Performance by Favouring Electrical Shortcuts. *Nat. Nanotechnol.* **2009**, *4*, 126–133.
6. Cellot, G.; Toma, F. M.; Varley, Z. K.; Laishram, J.; Villari, A.; Quintana, M.; Cipollone, S.; Prato, M.; Ballerini, L. Carbon Nanotube Scaffolds Tune Synaptic Strength in Cultured Neural Circuits: Novel Frontiers in Nanomaterial−Tissue Interactions. *J. Neurosci.* **2011**, *3*, 12945–12953.
7. Hai, A.; Dormann, A.; Shappir, J.; Yitzchaik, S.; Bartic, C.; Borghs, G.; Langedijk, J. P.; Spira, M. E. Spine-Shaped Gold Protrusions Improve the Adherence and Electrical Coupling of Neurons with the Surface of Micro-Electronic Devices. *J. R. Soc. Interface* **2009**, *6*, 1153–1165.
8. Malarkey, E. B.; Fisher, K. A.; Bekyarova, E.; Liu, W.; Haddon, R. C.; Parpura, V. Conductive Single-Walled Carbon Nanotube Substrates Modulate Neuronal Growth. *Nano Lett.* **2009**, *9*, 264–268.
9. Sorkin, R.; Greenbaum, A.; David-Pur, M.; Anava, S.; Ayali, A.; Ben-Jacob, E.; Hanein, Y. Process Entanglement as a Neuronal Anchorage Mechanism to Rough Surfaces. *Nanotechnology* **2009**, *20*, 015101.
10. Cho, Y.; Borgens, R. B. The Effect of an Electrically Conductive Carbon Nanotube/Collagen Composite on Neurite Outgrowth of PC12 Cells. *J. Biomed. Mater. Res. A* **2010**, *95*, 510–517.
11. Tosun, Z.; McFetridge, P. S. A Composite SWNT-Collagen Matrix: Characterization and Preliminary Assessment as a Conductive Peripheral Nerve Regeneration Matrix. *J. Neural. Eng.* **2010**, *7*, 066002.
12. Dvir, T.; Timko, B. P.; Kohane, D. S.; Langer, R. Nanotechnological Strategies for Engineering Complex Tissues. *Nat. Nanotechnol.* **2011**, *6*, 13–22.
13. Gelain, F.; Panseri, S.; Antonini, S.; Cunha, C.; Donega, M.; Lowery, J.; Taraballi, F.; Cerri, G.; Montagna, M.; Baldissera, F.; *et al.* Transplantation of Nanostructured Composite Scaffolds Results in the Regeneration of Chronically Injured Spinal Cords. *ACS Nano* **2011**, *5*, 227–236.
14. Cukierman, E.; Pankov, R.; Stevens, D. R.; Yamada, K. M. Taking Cell-Matrix Adhesions to the Third Dimension. *Science* **2001**, *294*, 1708–1712.
15. Discher, D. E.; Janmey, P.; Wang, Y. L. Tissue Cells Feel and Respond to the Stiffness of Their Substrate. *Science* **2005**, *310*, 1139–1143.
16. Geiger, B.; Spatz, J. P.; Bershadsky, A. D. Environmental Sensing through Focal Adhesions. *Nat. Rev. Mol. Cell. Biol.* **2009**, *10*, 21–33.
17. Mitragotri, S.; Lahann, J. Physical Approaches to Biomaterial Design. *Nat. Mater.* **2009**, *8*, 15–23.
18. Place, E. S.; Evans, N. D.; Stevens, M. M. Complexity in Biomaterials for Tissue Engineering. *Nat. Mater.* **2009**, *8*, 457–470.
19. Brunetti, V.; Maiorano, G.; Rizzello, L.; Sorce, B.; Sabella, S; Cingolani, R.; Pompa, P. P. Neurons Sense Nanoscale Roughness with Nanometer Sensitivity. *Proc. Natl. Acad. Sci. U.S.A.* **2010**, *107*, 6264–6269.
20. Stevens, M. M.; George, J. H. Exploring and Engineering the Cell Surface Interface. *Science* **2005**, *310*, 1135–1138.
21. Curtis, A. S.; Dalby, M.; Gadegaard, N. Cell Signaling Arising from Nanotopography: Implications for Nanomedical Devices. *Nanomedicine* **2006**, *1*, 67–72.
22. Krishnan, A.; Dujardin, E.; Ebbesen, T. W.; Yianilos, P. N.; Treacy, M. M. J. Young's Modulus of Single-Walled Nanotubes. *Phys. Rev. B* **1998**, *58*, 14013–14019.
23. Keefer, E. W.; Botterman, B. R.; Romero, M. I.; Rossi, A. F.; Gross, G. W. Carbon Nanotube Coating Improves Neuronal Recordings. *Nat. Nanotechnol.* **2008**, *3*, 434–439.
24. Kotov, N. A.; Winter, J. O.; Clements, I. P.; Jan, E.; Timko, B. P.; Campidelli, S.; Pathak, S.; Mazzatenta, A.; Lieber, C. M.; Prato, M.; *et al.* Nanomaterials for Neural Interfaces. *Adv. Mater.* **2009**, *21*, 3970–4004.
25. Shoval, A.; Adams, C.; David-Pur, M.; Shein, M.; Hanein, Y.; Sernagor, E. Carbon Nanotube Electrodes for Effective Interfacing with Retinal Tissue. *Front. Neuroeng.* **2009**, *2*, 4.
26. Mattson, M. P.; Haddon, R. C.; Rao, A. M. Molecular Functionalization of Carbon Nanotubes and Use as Substrates for Neuronal Growth. *J. Mol. Neurosci.* **2000**, *14*, 175–182.
27. Hu, H.; Ni, Y.; Montana, V.; Haddon, R. C.; Parpura, V. Chemically Functionalized Carbon Nanotubes as Substrates for Neuronal Growth. *Nano Lett.* **2004**, *4*, 507–511.
28. Lovat, V.; Pantarotto, D.; Lagostena, L.; Cacciari, B.; Grandolfo, M.; Righi, M.; Spalluto, G.; Prato, M.; Ballerini, L. Carbon Nanotube Substrates Boost Neuronal Electrical Signaling. *Nano Lett.* **2005**, *5*, 1107–1110.
29. Ni, Y.; Hu, H.; Malarkey, E. B.; Zhao, B.; Montana, V.; Haddon, R. C.; Parpura, V. Chemically Functionalized Water Soluble Single-Walled Carbon Nanotubes Modulate Neurite Outgrowth. *J. Nanosci. Nanotechnol.* **2005**, *5*, 707–712.
30. Massobrio, G.; Massobrio, P.; Martinoia, S. Modeling the Neuron-Carbon Nanotube-ISFET Junction To Investigate

the Electrophysiological Neuronal Activity. *Nano Lett.* **2008**, *8*, 4433–4440.
31. Pogodin, S.; Baulin, V. A. Can a Carbon Nanotube Pierce through a Phospholipid Bilayer? *ACS Nano* **2010**, *4*, 5293–5300.
32. Gähwiler, B. H.; Capogna, M.; Debanne, D.; McKinney, R. A.; Thompson, S. M. Organotypic Slice Cultures: A Technique Has Come of Age. *Trends Neurosci.* **1997**, *20*, 471–477.
33. Avossa, D.; Rosato-Siri, M. D.; Mazzarol, F.; Ballerini, L. Spinal Circuits Formation: A Study of Developmentally Regulated Markers in Organotypic Cultures of Embryonic Mouse Spinal Cord. *Neuroscience* **2003**, *122*, 391–405.
34. Avossa, D.; Grandolfo, M.; Mazzarol, F.; Zatta, M.; Ballerini, L. Early Signs of Motoneuron Vulnerability in a Disease Model System: Characterization of Transverse Slice Cultures of Spinal Cord Isolated from Embryonic ALS Mice. *Neuroscience* **2006**, *138*, 1179–1194.
35. Spenger, C.; Braschler, U. F.; Streit, J.; Lüscher, H. R. An Organotypic Spinal Cord–Dorsal Root Ganglion–Skeletal Muscle Coculture of Embryonic Rat. I. The Morphological Correlates of the Spinal Reflex Arc. *Eur. J. Neurosci.* **1991**, *3*, 1037–1053.
36. Galante, M.; Nistri, A.; Ballerini, L. Opposite Changes in Synaptic Activity of Organotypic Rat Spinal Cord Cultures after Chronic Block of AMPA/Kainite or Glycine and $GABA_A$ Receptors. *J. Physiol.* **2000**, *523*, 639–651.
37. Yabe, J. T.; Pimenta, A.; Shea, T. B. Kinesin-Mediated Transport of Neurofilament Protein Oligomers in Growing Axons. *J. Cell. Sci.* **1999**, *112*, 3799–3814.
38. Streit, J.; Spenger, C.; Lüscher, H. R. An Organotypic Spinal Cord–Dorsal Root Ganglion–Skeletal Muscle Coculture of Embryonic Rat. II. Functional Evidence for the Formation of Spinal Reflex Arcs *in Vitro*. *Eur. J. Neurosci.* **1991**, *3*, 10504–1068.
39. Cross, S. E.; Jin, Y.-S.; Rao, J.; Gimzewski, J. K. Nanomechanical Analysis of Cells from Cancer Patients. *Nat. Nanotechnol.* **2007**, *2*, 780–783.
40. Streit, J. Regular Oscillations of Synaptic Activity in Spinal Networks *in Vitro*. *J. Neurophysiol.* **1993**, *70*, 871–878.
41. Ballerini, L.; Galante, M. Network Bursting by Organotypic Spinal Slice Cultures in the Presence of Bicuculline and/or Strychnine Is Developmentally Regulated. *Eur. J. Neurosci.* **1998**, *10*, 2871–2879.
42. Furlan, F.; Taccola, G.; Grandolfo, M.; Guasti, L.; Arcangeli, A.; Nistri, A.; Ballerini, L. ERG Conductance Expression Modulates the Excitability of Ventral Horn GABAergic Interneurons That Control Rhythmic Oscillations in the Developing Mouse Spinal Cord. *J. Neurosci.* **2007**, *27*, 919–928.
43. Jonas, P. The Time Course of Signaling at Central Glutamatergic Synapses. *New Physiol. Sci.* **2000**, *15*, 83–89.
44. Rastaad, M.; Storm, J. F.; Andersen, P. Putative Single Quantum and Single Fibre Excitatory Postsynaptic Currents Show Similar Amplitude Range and Variability in Rat Hippocampal Slices. *Eur. J. Neurosci.* **1992**, *4*, 113–117.
45. Gaillard, C.; Cellot, G.; Li, S.; Toma, F. M.; Dumortier, H.; Spalluto, G.; Cacciari, B.; Prato, M.; Ballerini, L.; Bianco, A. Carbon Nanotubes Carrying Cell-Adhesion Peptides Do Not Interfere with Neuronal Functionality. *Adv. Mater.* **2009**, *21*, 2903–2908.
46. Cellot, G.; Ballerini, L.; Prato, M.; Bianco, A. Neurons Are Able To Internalize Soluble Carbon Nanotubes: New Opportunities or Old Risks? *Small* **2010**, *6*, 2630–2633.
47. Fabbro, A.; Toma, F. M.; Cellot, G.; Prato, M.; Ballerini, L. Carbon Nanotubes and Neuronal Performance. In *Nanomedicine and the Nervous System*; Science Publishers: Enfield, 2011; in press.
48. Zhou, X.; Moran-Mirabal, J. M.; Craighead, H. G.; McEuen, P. L. Supported Lipid Bilayer/Carbon Nanotube Hybrids. *Nat. Nanotechnol.* **2007**, *2*, 185–190.
49. Bianco, A.; Kostarelos, K.; Prato, M. Making Carbon Nanotubes Biocompatible and Biodegradabile. *Chem. Commun.* **2011**, *47*, 10182–10188.
50. Lee, H. J.; Park, J.; Yoon, O. J.; Kim, H. W.; Lee, D. Y.; Kim, D. H.; Lee, W. B.; Lee, N.-E.; Bonventre, J. V.; Kim, S. S. Amine-Modified Single-Walled Carbon Nanotubes Protect Neurons from Injury in a Rat Stroke Model. *Nat. Nanotechnol.* **2011**, *6*, 121–125.
51. Al-Jamal, K. T.; Gherardini, L; Bardi, G.; Nunes, A.; Guo, C.; Bussy, C.; Herrero, M. A.; Bianco, A.; Prato, M.; Kostarelos, K.; *et al.* Functional Motor Recovery from Brain Ischemic Insult by Carbon Nanotube-Mediated SiRNA Silencing. *Proc. Natl. Acad. Sci. U.S.A.* **2011**, *108*, 10952–10957.
52. Furlan, F.; Guasti, L.; Avossa, D.; Becchetti, A.; Cilia, E.; Ballerini, L.; Arcangeli, A. Interneurons Transiently Express the ERG K^+ Channels during Development of Mouse Spinal Networks *in Vitro*. *Neuroscience* **2005**, *135*, 1179–1192.
53. Cappella, B.; Dietler, G. Force–Distance Curves by Atomic Force Microscopy. *Surf. Sci. Rep.* **1999**, *34*, 1–104.
54. Butt, H. J.; Cappella, B. Force Measurements with the Atomic Force Microscope: Technique, Interpretation and Applications. *Surf. Sci. Rep.* **2005**, *59*, 1–152.
55. Rosato-Siri, M.; Grandolfo, M.; Ballerini, L. Activity-Dependent Modulation of GABAergic Synapses in Developing Rat Spinal Networks *in Vitro*. *Eur. J. Neurosci.* **2002**, *16*, 2123–2135.
56. Clements, J. D.; Bekkers, J. M. Detection of Spontaneous Synaptic Events with an Optimally Scaled Template. *Biophys. J.* **1997**, *73*, 220–229.